MATERIALS SCIENCE

Instant interfacial self-assembly for homogeneous nanoparticle monolayer enabled conformal "lift-on" thin film technology

Liping Song[1,2,3]†, Ben Bin Xu[4]†, Qian Cheng[2], Xiaoyuan Wang[1], Xiaoning Luo[1], Xue Chen[4], Tao Chen[2], Youju Huang[1]*

Thin film fabrication is of great importance in modern engineering. Here, we propose a universal and conformal thin film technique enabled by the wetting empowered interfacial self-assembly. By tailoring the contact angle of nanoparticle (NP), a NP monolayer can be assembled instantly (within 5 seconds) with an excellent harvesting efficiency (up to 97.5 weight %). This self-assembly strategy presents a universal applicability on various materials, e.g., nonmetal, metal, and core-shell structures, and can achieve a monolayer with same in-plane area as a 95 cm^2 wafer in a single process, indicating great potential for scale-up manufacturing. Through a template transfer, we coat the surface of different substrates (plastic, paper, etc.) with the assembled film in a conformal and non-destructive "lift-on" manner and subsequently demonstrate fluorescent micropatterns. This self-assembly strategy has great implications in advancing thin film technology in a user-friendly and cost-effective fashion for applications in anti-counterfeiting, actuators, and wearable/flexible electronics.

INTRODUCTION

Thin film engineering technique plays key role in the development of frontier electronics devices, by realizing micro/nano structures with unique optical, electrical, magnetic, and catalytic properties (1). Conventional micro- and nanofabrication methods for thin film engineering include top-down and bottom-up approaches. The lithography-based top-down strategy features high resolution and reliability (2) but has shortcomings such as high cost, time-consuming, etc. (3). The bottom-up approach contains diverse technical routes, i.e., template-based processes, laser printing, self-assembly, chemical vapor deposition, etc. (4). However, issues such as restrictive material systems, limited scalability, and additional processing constraints severely bottleneck the application of many of these approaches in scale-up manufacturing (5).

The conformal fabrication of thin film structure is of vital importance in enabling novel structure-property relationships (6) by fulfilling dedicated geometries for the robust sensing performances of flexible electronics (7). The versatile construction of two-dimensional (2D) micro-/nanostructures is highly desirable in designing and developing advanced electronic and optical devices with outstanding characteristics and functionalities (8). Several technologies are well established for achieving conformal 2D thin film patterning either in benchtop process or in scale-up manufacturing, such as subtractive lithography, laser direct writing, and transfer printing (9).

However, considerable challenges remain yet to be addressed, such as the stamp deformation, geometry-related stress localization, and the inaccurate controllability of motion and pressure (10).

Spontaneously, self-assembly of molecules or particles into 2D/3D architectures (11, 12) has emerged as an effective thin film process with advantages such as low cost, good compatibility with existing technology, and minimal infrastructure requirements. Recent development of 2D nanoparticle (NP) assemblies with surface tunability (13) enables promising application opportunities such as skin-like multifunctional wearable systems (14). Further explorations have focused on improving the efficiency to construct 2D thin films, through destabilization-based assembly (15), external-force assistance (16), and chemical linker–induced assembly (17). One of the latest technical trends is the interfacial assembly process, where NPs are drawn to low-tension interfaces by manipulating the surface charge density (18, 19). Substantial efforts have been exercised to improve the efficiency of interfacial assembly by tailoring the contact angle of NPs. Typical strategies include adding active solvents (20) and/or electrolytes (21), as well as hydrophobic modification (22). The core of these traditional interfacial assembly approaches is to reduce surface charge density on Au NPs by leveraging the low dielectric constant of ethanol as a solvent to overcome the kinetic energy barrier. Traditional interfacial assembly approaches have been constrained markedly by the limited reduction energy barrier (G_1) caused by the inadequate hydrophobicity on NPs (the contact angle of NPs, $\theta_1 < 90°$), which leads to several shortcomings such as the time-consuming assembly process (>20 min), limited assembly area (several square centimeters), inhomogeneous NP arrangement, and poor availability of NPs. Huge gap needs to be bridged to achieve scalable interfacial assembly of 2D NP film on interface.

Theoretically, the segregation of NPs to the interface needs to overcome the thermodynamic and kinetic energy barriers. Thermodynamically, assembly occurs autonomously due to the constant negative value of the Gibbs free energy (ΔE) that can be tuned by adjusting the contact angle (θ) of the NPs (23, 24)

[1]College of Material, Chemistry and Chemical Engineering, Key Laboratory of Organosilicon Chemistry and Material Technology, Ministry of Education, Hangzhou Normal University, Hangzhou 311121, China. [2]Key Laboratory of Marine Materials and Related Technologies, Zhejiang Key Laboratory of Marine Materials and Protective Technologies, Ningbo Institute of Materials Technology and Engineering, Chinese Academy of Sciences, Ningbo 315201, China. [3]National Synchrotron Radiation Laboratory, CAS Key Laboratory of Soft Matter Chemistry, Anhui Provincial Engineering, Laboratory of Advanced Functional Polymer Film, University of Science and Technology of China, Hefei 230026, China. [4]Mechanical and Construction Engineering, Faculty of Engineering and Environment, Northumbria University, Newcastle upon Tyne NE1 8ST, UK.
*Corresponding author. Email: yjhuang@hznu.edu.cn
†These authors contributed equally to this work.

$$\Delta E = -\pi r^2 \gamma_{\alpha\beta}(\cos\theta - 1)^2 \qquad (1)$$

where r is the radius and $\gamma_{\alpha\beta}$ is the interfacial tension of NP. Without any assistance, the assembly will be easily obstructed in most scenarios because of the strong dominance of the kinetic adsorption barrier (G) (22), which consists of the common contribution of NP interaction (G_{DLVO}) and hydrophobic interaction energy (G_{hydro}) (25)

$$G = G_{DLVO} + G_{hydro}(h) \qquad (2)$$

The hydrophobic interaction energy in Eq. 2 can be represented by

$$G_{hydro}(h) = -(K_{132}r)/h \qquad (3)$$

where h is the distance between NPs and interface; K_{132} is hydrophobic energy constant that can be determined by (26)

$$\log K_{132} = -8.2\left(\frac{\cos\theta - 1}{2}\right) - 20 \qquad (4)$$

Theoretically, a higher contact angle of NPs (>90°) yields a higher value of K (Eq. 4), thus leading to a lower G_{hydro} (Eq. 3) and G (Eq. 2). From this perspective, the value of θ is a critical factor to minimize both the thermodynamic and kinetic energy barriers, paving the road toward more effective thin film manufacturing techniques based on interfacial self-assembly.

Perfluorinated molecules with low surface free energy (27) hold great promise for interfacial self-assembly with the capability to effectively tune the wettability of NPs. Here, we report a universal and conformal thin film technique enabled by the versatile and robust interfacial assembly strategy by introducing perfluoro sulfhydryl ligand [perfluorodecanethiol (PFT)] (28). PFT provides abundant superhydrophobic structure (—CF$_3$) to endow NPs with super high contact angle to achieve an ultralow kinetical adsorption barrier (G_2; Fig. 1A). The interfacial assembly procedure in this work is illustrated in Fig. 1B, and the rapid assembly is achieved by adding the PFT mixing solution (ethanol/hexane). We manage to reduce the energy barrier powerfully ($\theta_2 > 130°$, $G_2 \ll G_1$) during assembly by inducing the strong hydrophobicity on the surface of Au NPs. Notably, the described interfacial self-assembly approach distinguishes itself with excellent potential for facile and scalable processing, including ultrafast assembly speed (less than 5 s) for fresh NPs, scale-up manufacturing (up to 95 cm^2 wafer size), remarkable assembly efficiency (up to 97.5%), and a universal applicability to a wide group of common materials (metals, polymer, oxides, and carbon materials). Moreover, the obtained monolayer films can be transferred with an embossing technique arbitrary on the substrates. In addition, the reorganization of assembled thin film was accomplished with interfacial capturing properties for hydrophilic molecules (fluorescent dyes) to achieve conformal fluorescence pattern in a "lift-on" manner.
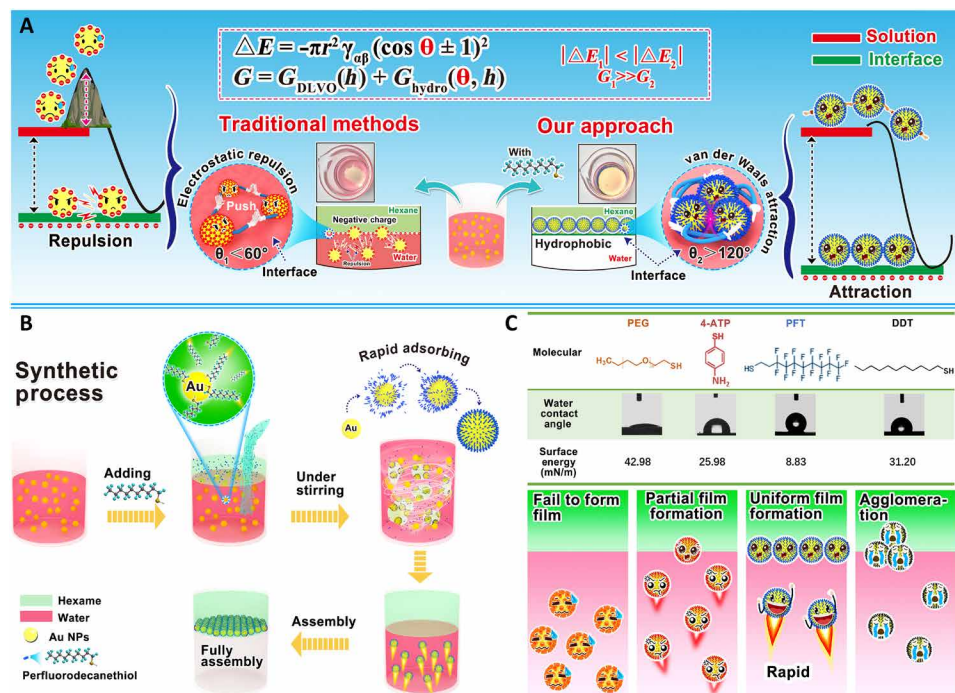

Fig. 1. Schematic illustration of instant interfacial assembly induced by PFT. (**A**) Core distinction between traditional approaches and our PFT-induced interfacial assembly. (**B**) Schematic representation and experimental demonstration for the rapid fabrication of scale-up and density assembly of NPs at interface induced by PFT. (**C**) Key low surface energy of PFT among many other molecules for interfacial assembly. PEG, polyethylene glycol; 4-Aminothiophenol (4-ATP), 4-adenosine 5′-triphosphate. Photo credit: Liping Song, College of Material, Chemistry and Chemical Engineering, Hangzhou Normal University.

RESULTS

Interfacial assembly of Au NPs into monolayer film

Here, PFT with rich hydrophobic perfluorinated group was used to overcome the thermodynamic and kinetic energy barriers superlatively (Fig. 1C and table S1). The Au NPs with a uniform size of 35 nm with customized surface properties (fig. S1) were prepared according to previously reported methods (29, 30). Unlike the traditional interfacial assembly strategy that usually requires complicated pretreatment for NPs (31), the fresh Au NPs with optimized concentration (figs. S2 and S3) in this work can be efficiently assembled into macroscopic 2D monolayer films without any modification. Considering the solvent system requirement for effective interfacial self-assembly (fig. S4) among the solvents with different types (fig. S4) and proportions (fig. S5), the facile assembly process can be achieved by rapidly shaking the mixture of PFT solution ($V_{Ethanol}$:V_{Hexane} = 2:1) and Au NP aqueous solution for less than 5 s (Fig. 2A and movie S1). This assembly approach offers an attractive potential for scale-up fabrication with a planar area up to 95 cm^2 (fig. S6). Different from the denoted "3D metal droplet" assemblies (32), the 2D film obtained by PFT-induced interfacial assembly presented single-storied, uniform, and dense NP arrangement (Fig. 2B and fig. S7). We also find that a higher concentration of PFT (around 10 mM) will lead to high contact angle of NPs (132°; Fig. 2C), thus resulting in a more homogeneous and denser 2D monolayer film at the end of assembly process (figs. S8 and S9). This can be attributed to the effective replacement of van der Waals force to electrostatic repulsion between PFT on Au NPs (33). The concentration effects of PFT on interfacial assembly have been exhibited in fig. S10. In addition, the assembled film has a redshift (about 77 nm) of plasmonic resonance compared to Au NP solution (curve a), which agrees with previously reported work (20).

We next assess the homogeneity of the self-assembled monolayer. The adsorption of the assembled monolayer film in ultraviolet-visible (UV-Vis) spectroscopy presents a sharp peak due to the formation of a homogeneous monolayer (Fig. 2D), while the Au NP film prepared through the conventional ethanol injection approach shows a board absorption peak (20) due to stacking and aggregation of the NPs. This is because the PFT effectively enhances and narrows the adsorption of the 2D Au NP films and the parallel samples manifested stable adsorption (fig. S11). The scale-up and density assembly of NP monolayer also enabled the high-optical reflectivity of the interface, as previously reported (16). In general, the optical mode of the interface transforms from transmission ("Window") to strong reflection ("Mirror") accompanying the interfacial assembling of NPs from the aqueous phase to interface (Fig. 2, E to I). The "seven-color flower" pattern was placed at the bottom of the aqueous dispersion of Au NPs. Initially, the pattern of the seven-color flower can be observed through the aqueous solution of Au NPs before assembly. After Au NP assembled film, the seven-color flower pattern almost disappears and is replaced with the "winter jasmine flower" pattern (pasted on the camera) (Fig. 2E-ii). In addition, we measure Grazing-Incidence Small-Angle X-ray Scattering (GISAXS) to confirm the ordered arrangement of 2D Au NP monolayer films, as shown in Fig. 2 (F and G). Multiple parallel streaks can be directly observed because of the distinct scattering of the monolayer superlattice (34). The prominent first- and second-order Bragg peaks determined by Gaussian fits (35) give insight that Au NPs were organized in macroscopic, dense, and short range–ordered assembly architectures. These results strongly demonstrate that the NP
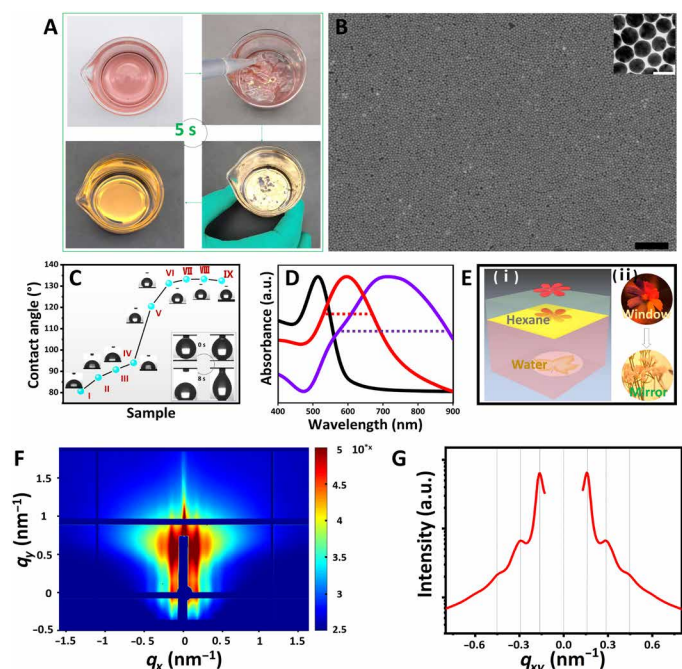
Fig. 2. 2D monolayer film of Au NPs with scale-up assembly area and dense NP arrangement. (**A**) Photographs of dynamic assembly process of Au NPs at water-hexane interface induced by PFT. (**B**) Scanning electron microscopy and transmission electron microscopy images of density Au NP assembled film. Scale bars, 500 and 20 nm, respectively. (**C**) Contact angles of pure silicon wafer (I) and Au NPs assemblies with different concentrations of PFT. The contact angle test was conducted by dropping 3 μl of water on the surface of Au NP films. The concentration of PFT from II to IX is 0 nM, 1 nM, 100 nM, 20 μM, 100 μM, 1 mM, 10 mM, and 100 mM, respectively. The insets are the snapshots of the dynamic process of dropping 3 μl of water on the surface of Au NP films formed with 10 mM PFT. (**D**) Ultraviolet–visible (UV-Vis) spectroscopy spectrum of Au NP solution (black) and Au NP assemblies acquired by conventional methods (purple) and PFT-assisted approach (red). a.u., arbitrary units. (**E**) Schematic (i) and real images (ii) observed before, after, and during violent mixing: the transferring from Window to Mirror. (**F**) 2D GISAXS image of Au NP assembled film. (**G**) 1D GISAXS patterns of Au NP assembled film converted from the 2D image. Photo credit: Liping Song, College of Material, Chemistry and Chemical Engineering, Hangzhou Normal University.

monolayer film is formed with high density and uniformity. By comparing this approach with other interfacial assembly strategies (table S2) in aspects such as film-forming time, pretreatment for NPs, assembly area, generalizability, NPs arrangement in films, etc., the described approach shows a superior efficiency with a much shorter assembly time (less than 5 s, at least one magnitude faster than the other approaches).

Our approach achieves a high utilization efficiency of NPs, with almost colorless aqueous solution after interfacial self-assembly (fig. S12C), compared to the usually pink or red residual solution of the conventional assembly method (fig. S12B) due to the large remaining quantity of NPs (31). The absorption (curve iii in Fig. 3A) of the bulk phase after film forming at 523 nm also directly verified the high utilization efficiency of NPs from bulk phase to interface. The average utilization efficiency of NPs with PFT up to 97.5% (curve ii in Fig. 3B) has been achieved, which is the most efficient assembly to date. The high utilization of NPs may be attributed to the distinctive hydrophobic attraction of the interface to PFT-coated NPs, while the incompatibility of PFT in hexane confines NPs in
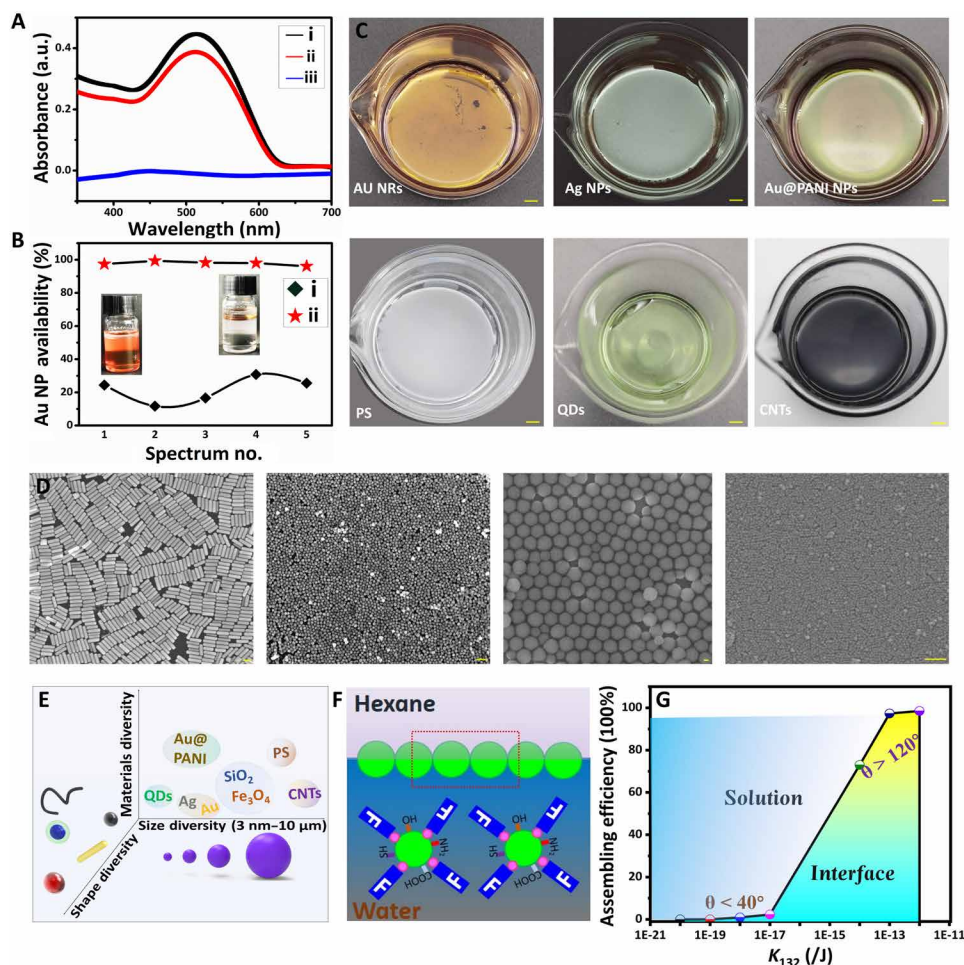
Fig. 3. The universality of PFT-dominated interfacial assembly approach. (**A**) UV-Vis spectra of Au NP solution before (curve i) and after assembly without (curve ii) and with PFT (curve iii). (**B**) Utilization statistics of Au NPs after assembly without PFT (curve i) and with PFT (curve ii). (**C**) Photographs of different materials assembled at interface. Scale bars, 1 cm. (**D**) Scanning electron microscopy images of different materials assembled at interface: Left to right: Au NRs, Ag NPs, SiO_2 microspheres, and Fe_3O_4, respectively. Scale bars, 100 nm. (**E**) Schematic diagram of the diversity of PFT-induced interfacial assembly. (**F**) Conjectural assembly mechanism diagram of nano- and microparticles without functional group to chemical covalence to PFT. (**G**) Phase diagram of different materials after assembly with PFT for evaluating the relationship between hydrophobicity and particle availability. Photo credit: Liping Song, College of Material, Chemistry and Chemical Engineering, Hangzhou Normal University.

monolayer construction. This approach provides a powerful platform for fabricating macroscopic and uniform monolayer arrays with the use of a small amount of NPs (0.49 mg of Au NPs on 17 cm^2). Our proposed thin film technology has vital importance in nanoengineering, especially using in nanomaterials with low production.

The ultralow surface energy of PFT enables uniform, rapid, and scale-up interfacial assembly of Au NPs, from the following three aspects: (i) facilitating ultralow surface energy for interfacial assembly, (ii) initiating a strong kinetical potential to drive the PFT-coated Au NPs to move to the interface (36), and (iii) achieving uniform and dense assembling of thin film on interface via van der Waals force between PFT (37). When adding PFT into Au NP aqueous solution (fig. S13), the PFT molecules are instantly changed from relatively stretchable state to collapsed state in the form of superhydrophobic beads with a size around 0.1 nm^2 alongside the diffusion of ethanol into water ($N_{ethanol}$:N_{water} = 1:5). This allows the PFT bonding to Au NPs by Au—S covalent interaction. Raman spectrum results identify the stretching vibration at 291 and 2137 cm^{-1} (curve c in fig. S14), which verifies the presence of Au—S covalent bond and

efficient attachment of PFT on Au NPs (38). On the basis of our calculation, a total amount of ca. 10^7 PFT molecules has been added in the solution of 10 ml to achieve NPs of 49 µg/ml. However, only ~10^4 PFT molecules (~ 0.1% of total amount in mixture) will be needed to cover the surface of Au NPs to induce the ultralow surface energy. Thus, most PFT molecules distribute in the water phase to reduce the hydrophobic interaction energy of the environment and initiate a strong kinetic potential to drive the PFT-coated Au NPs to move to the interface rapidly. Once Au NPs reach the water-hexane interface, the van der Waals force between PFT molecules (36) from neighboring Au NPs stabilizes and coordinates each NP in lattice structure to form the monolayer. The interfacial self-assembly of NPs into monolayer is systematically investigated as a function of the addition of PFT, and the surface hydrophobicity results in Fig. 2C show the robustness of the obtained Au NP films. Stable contact angle values are achieved at around 132° when we have PFT concentrations from 100 µM to 100 mM in the mixture, which indicate a threshold amount of 100 µM to acquire complete attachment of PFT on Au NPs.

Universal applicability of PFT dominated interfacial assembly to other NPs

This interfacial self-assembly strategy shows universal applicability to a wider group of materials such as metal NPs [Au nanorods (Au NRs) and Ag NPs] and their composites, Au NPs-Polyaniline (Au NPs@PANI) core-shell NPs, quantum dots (QDs), carbon nanotubes (CNTs), polystyrene (PS) microparticles, as well as Fe_3O_4 and SiO_2 NPs (Fig. 3C and fig. S15). High-quality films are achieved for most of particles with uniform and dense morphology (Fig. 3D and fig. S16). This interfacial assembly approach is independent of particle morphology, size, species, surface properties [zeta potentials ranging from −57 mV for Ag NPs (fig. S17) to 50 mV for hexadecyltrimethylammonium chloride (CTAC)–Au NPs (fig. S1)], and diversity functional groups (table S3). In addition, the assembly approach exhibited a wide distribution in size and shape (Fig. 3E). Unlike Au NPs, there is no impregnable covalent bond between PFT and nonmetallic NPs such as polymer and core-shell nanomaterials. There are three possibilities to be responsible for the film formation: (i) the affinity of the sulfhydryl group on PFT to the functional groups on particles. When adding PFT solution, particles will bind to them by hydrophilic affinity and move to the hexane-water interface (Fig. 3F). For example, we achieve high-quality, uniform, and dense-assembling structures with PFT on both PS microparticles and Au NPs@PANI. However, aggregations are found on the bottom of containers when replacing PFT (with —SH as functional group) with perfluoro-1-decanol (with —OH as functional group) (fig. S18). (ii) The extremely low surface energy (6.7 mJ/m^2 for —CF₃) of PFT (39) could decrease the adsorption barrier markedly and allow the PFT move to the interface during the assembly, creating a strong attraction for particles. (iii) Massive PFT distributing in solution to initiate a strong kinetical potential to drive the PFT-coated nano/microparticles to interface.

To offer a quantified measure, we construct a phase diagram for assembly efficiency of different materials as a function of hydrophobic energy constant (K_{132}; Fig. 3G), which plays determining role for the value of hydrophobic interaction energy (G_{hydro}). In general, Au NPs modified with hydrophilic ligands often present ultralow assembly efficiency (≤1.3%) due to their low contact angles (≤40°) and low hydrophobic interaction energy ($K_{132} \leq 10^{-17}$ J). The difficulty for assembly may be attributed to the high kinetical adsorption barrier of the NPs enabled by the strong and unshakable hydrophilic sulfhydryl ligands. For noble metal NPs without modification (such as Au NPs, Au NRs, and Ag NPs), the utilization efficiencies of the NPs were up to 99% due to their high contact angle (≥120°) and hydrophobic interaction energy ($K_{132} \geq 10^{-14}$ J). For nonmetal particles such as core-shell Au NPs@PANI and PS microspheres, the assembling efficiencies were about 75% due to their large size and relatively low hydrophobic energy ($K_{132} = 10^{-15}$ to 10^{-14} J). Thus, the assembly efficiency can be roughly predicted by assessing the contact angle and surface chemistry of NPs.

Conformal lift-on transferring of 2D monolayer films

Lithography-based thin film fabrication, a widely used technique in microdevice engineering (40), has ongoing limitations such as the high process cost and the use of complicated template (41). In this work, scale-up assembly of NPs in 2D films provides an alternative by coating 2D monolayer film on arbitrary substrate via a two-step process (42). As illustrated in Fig. 4A, 2D Au NP monolayer films can be transferred straightforwardly via a lift-on process using the
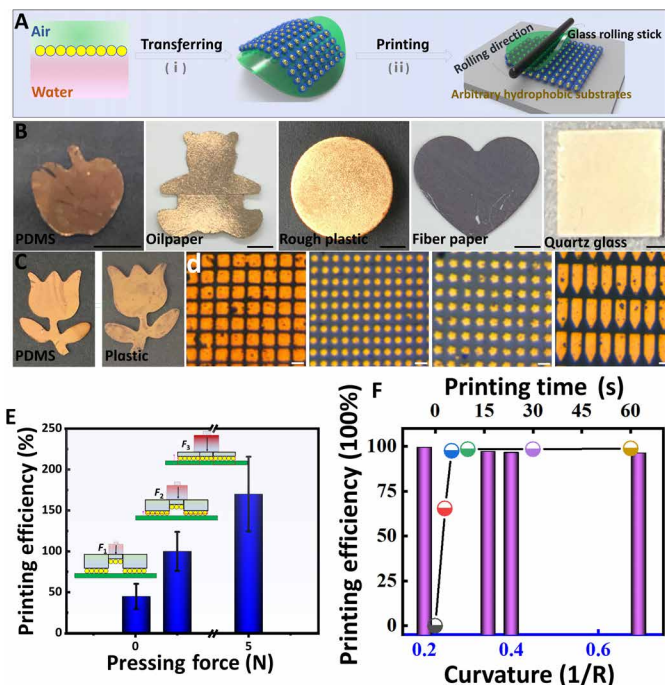
Fig. 4. The conformal coating of assembled monolayer film on various substrates. (**A**) Schematic diagram of transferring and printing of Au NP assembled films. (**B**) Photographs of Au NP assembled films transferring on various hydrophilic and hydrophobic substrates. Scale bars, 0.5 cm. Printing 2D Au NP films on PDMS with macroscopic (**C**) and micropatterned (**D**) Au NP films on glass substrate. Scale bars, 10 μm. (**E**) Estimated printing efficiency of Au NP films on glass with different press pressures. (**F**) Estimated printing efficiency of Au NP films micropatterns on glass with different print times and shapes. Photo credit: Liping Song, College of Material, Chemistry and Chemical Engineering, Hangzhou Normal University.

substrate to lift the free-standing 2D films on water surface ranging from hydrophobic oilpaper (120°) to hydrophilic quartz glass (45°) (Fig. 4B). 2D monolayer films fit nicely with nearly arbitrary substrate via Langmuir-Blodgett transfer technique (20) despite the high hydrophobicity (Fig. 2C). We can even achieve multilayer films by repeatedly transferring Au NP monolayer (fig. S19); however, dedicated accessories/equipment will be needed to ensure a good dimensional alignment when applying this strategy to create structures. Printing large-scale thin film on target substrate can be accomplished by exerting appropriate force on Au NP film (Fig. 4C). We also find that the micropattern of the thin film from polydimethylsiloxane (PDMS) can be retained entirely on glass (Fig. 4D).

To understand the transfer mechanism, we next model the system as a laminated structure composed of three layers: (i) glass substrate, (ii) Au monolayer, and (iii) PDMS stamp (see fig. S20). The transfer process depends on the competing adhesion at the two interfaces in the structure. To quantify the strength of adhesion, we use a critical energy release rate G_c. G_c accounts for the energy release when the interfacial bond is broken and the energy dissipation around the crack tip (43). Therefore, higher G_c corresponds to higher adhesive strength. By comparing the critical energy release rates at the Au/glass interface ($G_c^{Au/glass}$) and the Au/PDMS interface ($G_c^{Au/PDMS}$), the criteria for pickup and printing processes can be obtained as (43):

For printing

$$G_c^{Au/glass} > G_c^{Au/PDMS} \qquad (5)$$

For pick up

$$G_c^{Au/glass} < G_c^{Au/PDMS} \qquad (6)$$

It is found in the literature that $G_c^{Au/PDMS}$ is around 4 J/m² at the low peeling rate (~0), which is smaller than the average $G_c^{Au/glass}$ around 12 J/m² (44). Therefore, for our quasi-static printing test (low peeling rate), criterion (Eq. 5) is satisfied, and the Au monolayer is transferred (printed) to the glass substrate (fig. S20). Moreover, to ensure the conformal contact between the Au monolayer and the substrate, we usually apply a gentle pressure on the laminated structure before peeling off the PDMS stamp. If the gentle pressure has not reached threshold, then the contact between Au monolayer and the substrate is ideal. In this case, $G_c^{Au/glass}$ is decreased since adhesion is dominated by van der Waals interactions (45), which diminish with increasing distance. As a result, criterion (Eq. 5) may not be satisfied, leading to a reduction in transferring (printing) efficiency. As shown in Fig. 4E and figs. S21 and S22, the printing efficiency presents a series of transformations from no Au NP films printed without press pressure (I), part of them printed (II, 0.01 N), totally printed (III, 0.5 N), and residuals between patterns printed (IV, 5 N). The effect of compressive force on the printing process is also investigated here, and it is found that a compressive force of 0.5 N is large enough to reach ~100% printing efficiency. Moreover, the transfer printing process in this work seems be independent of the shape of micropatterns and printing time. Some micropatterns with sharp shape (curvature up to 0.7; Fig. 4F) and different layouts (fig. S23) can also be successfully printed without any vestiges. Practically, we find that several possibilities intriguingly enable the transferring and high-resolution printing of Au NP films as follows: (i) Ethanol bridged the Au NP films at interface with substrate considering the low surface tension of ethanol (22.1 mN/m). It is found that the transferring efficiency of Au NP films to substrate suffered great impact after vaporizing ethanol at high temperature (fig. S24). (ii) The hydrogen bond interaction between —C—F and —OH or —HX of substrate (46, 47) is conducive to transfer and print Au NP films. As a result, the Au NP films on silicon wafer with/without plasma treatment show distinguishing printing performance (fig. S25). (iii) The large surface area and the relative mechanical stability of Au NP monolayer (48) provide convenience (movie S2) for the transferring of Au NP films. In addition, integrating substrate to the air side of Au NP films is more suitable for obtaining conformal Au NP films considering the hydrophobicity mismatches (fig. S26).

Demonstration of the fluorescent pattern based on the lift-on transferring of assembled film

The conformal functional optical patterning holds promises for various applications, such as soft electronics, solar cells, and anti-counterfeiting
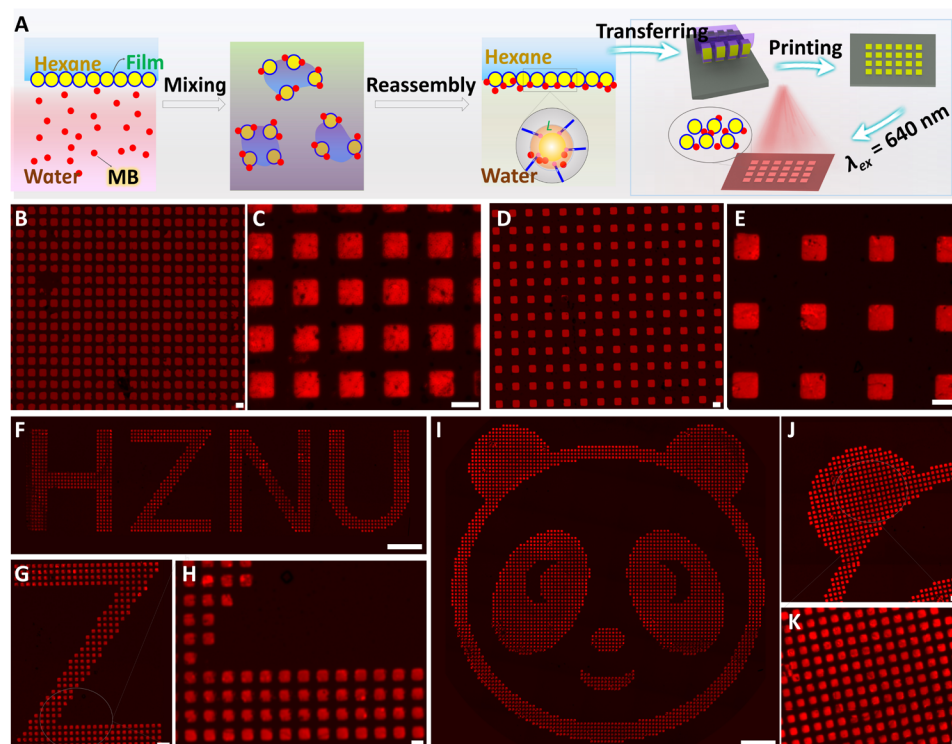
Fig. 5. The printing abilities of composite films for constructing fluorescent security micropatterns. (A) Schematic diagram of adsorbing fluorescent dyes (MB) via self-healing 2D Au NP monolayer films and the printing of patterned fluorescent security labels. (B to E) Fluorescent images of self-assembled micropatterns printed on glass from PDMS with different spacings. Scale bars, 10 μm. (F and G) Fluorescent image of micropatterned letter HZNU and its local enlarged images. Scale bars, 100, 20, and 5 μm (F, G, and H, respectively). (I to K) Fluorescent image of micropatterned panda and its local enlarged images. Scale bars, 100, 20, and 5 μm (I, J, and K, respectively). Photo credit: Liping Song, College of Material, Chemistry and Chemical Engineering, Hangzhou Normal University.

security labels *(49)*. However, the traditional printing technologies often suffer high cost, limited pattern area, low universality, low efficiency in integrating the fluorescent/optical indicator layer, and low throughput in mass production *(50)*. In this work, the Au NP films at the hexane-water interface exhibited outstanding anti-interference performance and excellent capturing/mixing feature to incorporating fluorescent molecules in the assembled monolayer. Unlike traditional interfacial assembled monolayers, the PFT-induced Au NP films exhibit the "self-healing" performance *(51)* as Au NPs reassembly at the interface instantaneously after intensively stirring (1500 rpm) the film-assembled hexane-water system (fig. S27). The energy equilibrium of the system will be restored when the kinetical adsorption barrier (*G*; Eq. 2) drives the PFT-coated Au NPs to interface to re-establish the surface tension difference between water phase and interface. A unique molecule mixing is fulfilled alongside this kinetical adsorption barrier-driving NP movement. The fluorescent dye molecules are captured and mixed with Au NPs and eventually embedded in the Au NP monolayer uniformly. As shown in Fig. 5A, a certain amount of fluorescent dye [methylene blue (MB)] in aqueous solution can be captured after reassembling 2D Au NP monolayer (fig. S28).

Thus, we believe that PFT-coated Au NP films pave a distinctive way to construct security labels with high uniformity, large scale, and high resolution. After being transferred on patterned PDMS in a lift-on manner, the composite film presents uniform and macroscopic assemblies. The chiseled micropattern with different spacings on glass is acquired (Fig. 5, B to E, and fig. S29). Note that the mismatching between the absorption of Au NPs (523 nm; Fig. 2C) and the fluorescent emission of MB (675 nm; fig. S28) effectively avoids the fluorescence interference between them. Apart from MB, Rhodamine 6G (R6G) can also be captured to interface for printing, and micropatterned features with sharp corners can be clearly observed without fluorescence signals (fig. S30). Capturing molecules at the interface should meet two necessary conditions: (i) relatively high concentration for molecules ($>10^{-6}$ M for MB and $>10^{-7}$ M for R6G) and (ii) a desired kinetic potential for Au NPs to effectively capture and take fluorescent dyes to the interface. We further print the fluorescence letters of "HZNU" (Fig. 5, F to H) and an image of "panda" (Fig. 5, I to K) that made up of micropattern (5 μm) by transferring from the designed PDMS (fig. S31). The resolution and contrast of pattern can be highly controllable as there is no fluorescence between the adjacent neighboring micropatterns, which is enabled by transferring the interfacial enhanced self-assembled PFT-coated NPs. This facile fabrication of thin film with high capturing efficiency, good printing accuracy, and universal applicability on the various substrates presents great potentials in the future application in scale-up soft electronics and distinguished anti-counterfeiting.

DISCUSSION

In summary, we describe an instant and universal interfacial self-assembly strategy through tuning the contact angle of NPs. This approach has been demonstrated to achieve scale up assembly (up to 95 cm²) within less than 5 s. This interfacial self-assembly approach exhibits high particle utilization efficiency up to 97.5% along with high film uniformity, as well as compatibility with a wide range of common materials. Moreover, it also enables a lift-on strategy facilitating transfer of thin film by transferring the self-assembled

monolayer onto arbitrary substrates. In addition to macroscopic and micropattern printing, with the assistance of molecule capturing properties, the thin film exhibits strong self-healing performance and functional fluorescent anti-counterfeiting properties. We believe that this unique thin film strategy will pave a way for adaptive, simple, highly distinguished soft electronics, and distinguished anti-counterfeiting applications.

MATERIALS AND METHODS
Materials
All chemicals were used as received without further purification. Gold (III) chloride trihydrate (HAuCl$_4$·3H$_2$O, ≥99.99%) was purchased from Sigma-Aldrich. Sodium citrate (SC; ≥99%), tris(hydroxymethyl) aminomethane (Tris Base, Guaranteed reagent), ethanol, R6G, MB, hexane (Guaranteed reagent), toluene, butyl alcohol, cyclohexane, dichloromethane, and methanol were obtained from Sinopharm Chemical Reagent Co., Ltd. (Shanghai, China). 1*H*,1*H*,2*H*,2*H*-perfluorodecthiol (>97%), 1*H*,1*H*,2*H*,2*H*-perfluoro-1-decanol, perfluorododecane (>97%), and 1*H*,1*H*,2*H*,2*H*-perfluorooctyltriethoxysilane (>96%) were purchased from J&K Scientific. Hexadecyltrimethyl-ammonium bromide (CTAB; >98.0%), CTAC (>98.0%). Mono-dispersed PS microspheres suspension (2 μm, 5 weight % in water) was obtained from Aladdin Biochemical Technology Co., Ltd. (Shanghai, China). The raw multiwall CNTs with a diameter of about 10 to 30 nm (>90%) was obtained from Chengdu Organic Chemistry Co. Ltd. Fe$_3$O$_4$ NPs (10 nm, 1 mg/ml) was purchased from Keeco Biotechnology Co. Ltd. (Nanjing, China). The patterned PDMS template was commercially available. All chemicals were used without further purification. Deionized water was used throughout the experiment process.

Synthesis of NPs
The CTAC–Au NPs were synthesized according to previous work *(29)* as follows: 50 μl of these CTAB seeds, ascorbic acid (1.5 ml, 100 mM), and CTAC (2.0 ml, 200 mM) were mixed at 600 rpm, followed by injecting HAuCl$_4$ (2.0 ml, 0.5 mM). After stirred for 15 min (300 rpm), the Au NPs were purified by centrifugation and further dispersed in CTAC (1.0 ml, 20 mM). These Au NP@CTAC were used as seeds to further synthesize Au NPs@CTAC with larger diameters: Au NPs@CTAC was purified by centrifugation and further dispersed in 20 mM CTAC. CTAC (20 ml, 100 mM) and the Au NPs@CTAC seeds with curtained volume (in 20 mM CTAC) were mixed and treated with ultrasound for 10 min. The mixture was stirred (400 rpm) in a water bath at 30°C by adding ascorbic acid (1.3 ml, 10 mM). After 1 min, HAuCl$_4$ (20 ml, 0.5 mM) was added into the mixture with a speed of 20 ml/hour. Then, the mixture was stirred (400 rpm) for another 10 min at 30°C, and the Au NPs@CTAC pellet was dispersed in the same volume of water after treating with centrifugation.

The SC–Au NPs were synthesized according to our previous work *(30)*: 140 ml of deionized water was heated until the temperature was constant at 137°C. Then, 10 ml of SC (33 mM) solution was added and stirred for 15 min. Then, 1 ml of fresh HAuCl$_4$ (25 mM) and 5 ml of Tris Base (0.1 M) solution were sequentially added (time delay, 60 s). The temperature of the oil bath was adjusted to 100°C after 20 min of continuous heating. Then, 1 ml of HAuCl$_4$ (25 mM) was injected an additional two times with an interval of 30 min to improve the shape and size uniformity of obtained Au NPs.

Ag NPs (52), Au NRs (53), Au NPs@PANI (54), QDs (55), and SiO$_2$-NH$_2$ (56) were all synthesized according to previous work. All NPs are monodispersed and fresh-prepared without any pretreatment.

Interfacial assembly of Au NPs

Five milliliters of newly Au NPs was placed into a 5-ml glass bottle. Then, the PFT solution (10 mM, 10 ml, $V_{ethanol}$:V_{hexane} = 2:1) was poured into the Au NP solution, oscillating 3 s and stewing 2 s to obtain density 2D Au NP monolayer films. The film-forming process of other materials is similar to the assembly procedure of Au NPs.

The printing of Au NP monolayer films

The printing of Au NP films on glass was achieved by applying a certain pressing force (~0.5 N) on clean and dry glass and keep for 15 s. The printing of Au NP–dye complexed films was achieved by similar methods.

Characterization techniques

UV-Vis absorption spectra were recorded by a TU-1810 UV-Vis spectrophotometer provided by Purkinje General Instrument Co. Ltd. The morphologies of Au NPs were investigated via an S-4800 (Hitachi, Japan) field-emission scanning electron microscope at an acceleration voltage of 4 kV. Transmission electron microscopy was performed on a JEOL JEM 2100 electron microscope operating at 200 kV. Raman spectra were collected on an R-3000HR spectrometer (Raman Systems Inc., R-3000 series) with a red light-emitting diode laser (532 nm). Laser power was 0.5% (1.4 mW). Contact angle pictures was carried out by a contact angle meter (DCAT21 and OCA25) using a 3-µl droplet of water as an indicator. The small-angle x-ray scattering (SAXS) experiments were performed at beamline BL16B1 of Shanghai Synchrotron Radiation Facility. The incident x-ray photon energy was 10 keV (wavelength = 0.124 nm). The beam size was 0.4 mm by 0.5 mm. The distance between the sample and the detector was set to 1.92 m. The scattering patterns were collected by a Pilatus 2M detector with pixel size of 172 µm by 172 µm. Micropattern fluorescence characterizations were conducted with Zeiss confocal laser fluorescence microcope (LSM-710, Germany).

SUPPLEMENTARY MATERIALS

Supplementary material for this article is available at https://science.org/doi/10.1126/sciadv.abk2852

REFERENCES AND NOTES

1. S. Zhang, C. I. Pelligra, X. Feng, C. O. Osuji, Directed assembly of hybrid nanomaterials and nanocomposites. *Adv. Mater.* **30**, 1705794 (2018).
2. T. Das Gupta, L. Martin-Monier, W. Yan, A. Le Bris, T. Nguyen-Dang, A. G. Page, K.-T. Ho, F. Yesilköy, H. Altug, Y. Qu, F. Sorin, Self-assembly of nanostructured glass metasurfaces via templated fluid instabilities. *Nat. Nanotechnol.* **14**, 320–327 (2019).
3. Y. Liu, K. Du, I. Wathuthanthri, W. Xu, C. H. Choi, Freestanding photoresist film: A versatile template for three-dimensional micro- and nanofabrication. *Adv. Funct. Mater.* **30**, 2004129 (2020).
4. C. Jia, Z. Lin, Y. Huang, X. Duan, Nanowire electronics: From nanoscale to macroscale. *Chem. Rev.* **119**, 9074–9135 (2019).
5. J. Chang, J. Lee, A. Georgescu, D. Huh, T. Kang, Generalized on-demand production of nanoparticle monolayers on arbitrary solid surfaces via capillarity-mediated inverse transfer. *Nano Lett.* **19**, 2074–2083 (2019).
6. R. C. Webb, A. P. Bonifas, A. Behnaz, Y. Zhang, K. J. Yu, H. Cheng, M. Shi, Z. Bian, Z. Liu, Y.-S. Kim, W.-H. Yeo, J. S. Park, J. Song, Y. Li, Y. Huang, A. M. Gorbach, J. A. Rogers, Ultrathin conformal devices for precise and continuous thermal characterization of human skin. *Nat. Mater.* **12**, 938–944 (2013).
7. J. Kim, A. S. Campbell, B. E.-F. de Avila, J. Wang, Wearable biosensors for healthcare monitoring. *Nat. Biotechnol.* **37**, 389–406 (2019).
8. M. Su, F. Qin, Z. Zhang, B. Chen, Q. Pan, Z. Huang, Z. Cai, Z. Zhao, X. Hu, D. Derome, J. Carmeliet, Y. Song, Non-lithography hydrodynamic printing of micro/nanostructures on curved surfaces. *Angew. Chem. Int. Ed.* **59**, 14234–14240 (2020).
9. Z. Yan, T. Pan, M. Xue, C. Chen, Y. Cui, G. Yao, L. Huang, F. Liao, W. Jing, H. Zhang, M. Gao, D. Guo, Y. Xia, Y. Lin, Thermal release transfer printing for stretchable conformal bioelectronics. *Adv. Sci.* **4**, 1700251 (2017).
10. Y. Huang, H. Wu, L. Xiao, Y. Duan, H. Zhu, J. Bian, D. Yeab, Z. Yin, Assembly and applications of 3D conformal electronics on curvilinear surfaces. *Mater. Horiz.* **6**, 642–683 (2019).
11. M. D. Scanlon, E. Smirnov, T. J. Stockmann, P. Peljo, Gold nanofilms at liquid-liquid interfaces: An emerging platform for redox electrocatalysis, nanoplasmonic sensors, and electrovariable optics. *Chem. Rev.* **118**, 3722–3751 (2018).
12. W. Zhao, S. Xiao, Y. Zhang, D. Pan, J. Wen, X. Qian, D. Wang, H. Cao, W. He, M. Quan, Z. Yang, Binary "island" shaped arrays with high-density hot spots for surface-enhanced Raman scattering substrates. *Nanoscale* **10**, 14220–14229 (2018).
13. J. B. Lee, H. Walker, Y. Li, T. W. Nam, A. Rakovich, R. Sapienza, Y. S. Jung, Y. S. Nam, S. A. Maier, E. Cortés, Template dissolution interfacial patterning of single colloids for nanoelectrochemistry and nanosensing. *ACS Nano* **14**, 17693–17703 (2020).
14. T. R. Ray, J. Choi, A. J. Bandodkar, S. Krishnan, P. Gutruf, L. Tian, R. Ghaffari, J. A. Rogers, Bio-integrated wearable systems: A comprehensive review. *Chem. Rev.* **119**, 5461–5533 (2019).
15. Y. Shin, J. Song, D. Kim, T. Kang, Facile preparation of ultrasmall void metallic nanogap from self-assembled gold-silica core-shell nanoparticles monolayer via kinetic control. *Adv. Mater.* **27**, 4344–4350 (2015).
16. Y. Montelongo, D. Sikdar, Y. Ma, A. J. S. McIntosh, L. Velleman, A. R. Kucernak, J. B. Edel, A. A. Kornyshev, Electrotunable nanoplasmonic liquid mirror. *Nat. Mater.* **16**, 1127–1135 (2017).
17. J. Kim, X. Song, F. Ji, B. Luo, N. F. Ice, Q. Liu, Q. Zhang, Q. Che, Polymorphic assembly from beveled gold triangular nanoprisms. *Nano Lett.* **17**, 3270–3275 (2017).
18. Y. J. Li, W. J. Huang, S. G. Sun, A universal approach for the self-assembly of hydrophilic nanoparticles into ordered monolayer films at a toluene/water interface. *Angew. Chem. Int. Ed.* **45**, 2537–2539 (2006).
19. W. Zhao, Y. Zhang, J. Yang, J. Li, Y. Feng, M. Quan, Z. Yang, S. Xiao, Synergistic plasmon resonance coupling and light capture in ordered nanoarrays as ultrasensitive and reproducible SERS substrates. *Nanoscale* **12**, 18056–18066 (2020).
20. S. Si, W. Liang, Y. Sun, J. Huang, W. Ma, Z. Liang, Q. Bao, L. Jiang, Facile fabrication of high-density sub-1-nm gaps from Au nanoparticle monolayers as reproducible SERS substrates. *Adv. Funct. Mater.* **26**, 8137–8145 (2016).
21. Y. Liu, Y. Liu, P. Tao, W. Shang, C. Song, T. Deng, Vertical segregation in the self-assembly of nanoparticles at the liquid/air interface. *Nanoscale* **6**, 14662–14666 (2014).
22. H. Tian, H. Li, Y. Fang, Binary thiol-capped gold nanoparticle monolayer films for quantitative surface-enhanced Raman scattering analysis. *ACS Appl. Mater. Interfaces* **11**, 16207–16213 (2019).
23. B. P. Binks, Particles as surfactants-similarities and differences. *Curr. Opin. Colloid Interface Sci.* **7**, 21–41 (2002).
24. Z. Niu, J. He, T. P. Russell, Q. Wang, Synthesis of nano/microstructures at fluid interfaces. *Angew. Chem. Int. Ed.* **49**, 10052–10066 (2010).
25. J.-W. Hu, G.-B. Han, B. Ren, S.-G. Sun, Z.-Q. Tian, Theoretical consideration on preparing silver particle films by adsorbing nanoparticles from bulk colloids to an air-water interface. *Langmuir* **20**, 8831–8838 (2004).
26. R.-H. Yoon, D. H. Flinn, Y. I. Rabinovich, Hydrophobic interactions between dissimilar surfaces. *J. Colloid Interface Sci.* **185**, 363–370 (1997).
27. Q. Sun, B. Aguila, J. A. Perman, T. Butts, F.-S. Xiao, S. Ma, Integrating superwettability within covalent organic frameworks for functional coating. *Chem* **4**, 1726–1739 (2018).
28. P. Sun, L. M. Nowack, W. Bu, M. K. Bera, S. Griesemer, M. Reik, J. Portner, S. A. Rice, M. L. Schlossman, B. Lin, Free thiols regulate the interactions and self-assembly of thiol-passivated metal nanoparticles. *Nano Lett.* **21**, 1613–1619 (2021).
29. F. Schulz, O. Pavelka, F. Lehmkühler, F. Westermeier, Y. Okamura, N. S. Mueller, S. Reich, H. Lange, Structural order in plasmonic superlattices. *Nat. Commun.* **11**, 3821 (2020).
30. X. Lu, Y. Huang, B. Liu, L. Zhang, L. Song, J. Zhang, A. Zhang, T. Chen, Light-controlled shrinkage of large-area gold nanoparticle monolayer film for tunable SERS activity. *Chem. Mater.* **30**, 1989–1997 (2018).
31. Y. Xu, M. P. Konrad, W. W. Lee, Z. Ye, S. E. J. Bell, A method for promoting assembly of metallic and nonmetallic nanoparticles into interfacial monolayer films. *Nano Lett.* **16**, 5255–5260 (2016).
32. Y. Xu, F. Yu, M. Su, S. Du, H. Liu, Halide-assisted activation of atomic hydrogen for photoreduction on two-liquid interfacial plasmonic arrays. *Chem. Commun.* **55**, 1422–1425 (2019).
33. Y.-K. Park, S. Park, Directing close-packing of midnanosized gold nanoparticles at a water/hexane interface. *Chem. Mater.* **20**, 2388–2393 (2008).

34. M. J. Campolongo, S. J. Tian, D.-M. Smilgies, M. Zhao, Y. Chen, I. Xhangolli, W. Cheng, D. Luo, Crystalline gibbs monolayers of DNA-capped nanoparticles at the air–liquid interface. *ACS Nano* **5**, 7978–7985 (2011).

35. L. Wu, X. Wang, G. Wang, G. Chen, In situ x-ray scattering observation of two-dimensional interfacial colloidal crystallization. *Nat. Commun.* **9**, 1335 (2018).

36. V. H. Dalvi, P. J. Rossky, Molecular origins of fluorocarbon hydrophobicity. *Proc. Natl. Acad. Sci. U.S.A.* **107**, 13603–13607 (2010).

37. O. Bjorneholm, M. H. Hansen, A. Hodgson, L.-M. Liu, D. T. Limmer, A. Michaelides, P. Pedevilla, J. Rossmeisl, H. Shen, G. Tocci, E. Tyrode, M.-M. Walz, J. Werner, H. Bluhm, Water at interfaces. *Chem. Rev.* **116**, 7698–7726 (2016).

38. Y. Yu, Y. Hong, P. Gao, M. K. Nazeeruddin, Glutathione modified gold nanoparticles for sensitive colorimetric detection of Pb^{2+} ions in rainwater polluted by leaking perovskite solar cells. *Anal. Chem.* **88**, 12316–12322 (2016).

39. S. Yang, X. Dai, B. B. Stogin, T. S. Wong, Ultrasensitive surface-enhanced Raman scattering detection in common fluids. *Proc. Natl. Acad. Sci. U.S.A.* **113**, 268–273 (2016).

40. M. Kim, D. Ha, T. Kim, Cracking-assisted photolithography for mixed-scale patterning and nanofluidic applications. *Nat. Commun.* **6**, 6247 (2015).

41. T. W. Park, M. Byun, H. Jung, G. Lee, J. H. Park, H.-I. Jang, J. Lee, S. Kwon, S. Hong, J.-H. Lee, Y. S. Jung, K. H. Kim, W. I. Park, Thermally assisted nanotransfer printing with sub–20-nm resolution and 8-inch wafer scalability. *Sci. Adv.* **6**, eabb6462 (2020).

42. J. Feng, L. Peng, C. Wu, X. Sun, S. Hu, C. Lin, J. Dai, J. Yang, Y. Xie, Giant moisture responsiveness of VS_2 ultrathin nanosheets for novel touchless positioning interface. *Adv. Mater.* **24**, 1969–1974 (2012).

43. A. Carlson, A. M. Bowen, Y. Huang, R. G. Nuzzo, J. A. Rogers, Transfer printing techniques for materials assembly and micro/nanodevice fabrication. *Adv. Mater.* **24**, 5284–5318 (2012).

44. X. Feng, M. A. Meitl, A. M. Bowen, Y. Huang, R. G. Nuzzo, J. A. Rogers, Competing fracture in kinetically controlled transfer printing. *Langmuir* **23**, 12555–12560 (2007).

45. M. A. Meitl, Z.-T. Zhu, V. Kumar, K. J. Lee, X. Feng, Y. Y. Huang, I. Adesida, R. G. Nuzzo, J. A. Rogers, Transfer printing by kinetic control of adhesion to an elastomeric stamp. *Nat. Mater.* **5**, 33–38 (2005).

46. Z.-Y. Cao, W. Wang, K. Liao, X. Wang, J. Zhou, J. Ma, Catalytic enantioselective synthesis of cyclopropanes featuring vicinal all-carbon quaternary stereocenters with a CH_2F group; study of the influence of C–F···H–N interactions on reactivity. *Org. Chem. Front.* **5**, 2960–2968 (2018).

47. J. S. Yu, Y. L. Liu, J. Tang, X. Wang, J. Zhou, Highly efficient "on water" catalyst-free nucleophilic addition reactions using difluoroenoxysilanes: Dramatic fluorine effects. *Angew. Chem. Int. Ed.* **53**, 9512–9516 (2014).

48. A. Dong, J. Chen, P. M. Vora, J. M. Kikkawa, C. B. Murray, Binary nanocrystal superlattice membranes self-assembled at the liquid-air interface. *Nature* **466**, 474–477 (2010).

49. X. Yu, L. Wu, D. Yang, M. Cao, X. Fan, H. Lin, Q. Zhong, Y. Xu, Q. Zhang, Hydrochromic $CsPbBr_3$ nanocrystals for anti-counterfeiting. *Angew. Chem. Int. Ed.* **59**, 14527–14532 (2020).

50. A. O. Larin, L. N. Dvoretckaia, A. M. Mozharov, I. S. Mukhin, A. B. Cherepakhin, I. I. Shishkin, E. I. Ageev, D. A. Zuev, Luminescent erbium-doped silicon thin films for advanced anti-counterfeit labels. *Adv. Mater.* **33**, e2005886 (2021).

51. L. Tian, M. Su, F. Yu, Y. Xu, X. Li, L. Li, H. Liu, W. Tan, Liquid-state quantitative SERS analyzer on self-ordered metal liquid-like plasmonic arrays. *Nat. Commun.* **9**, 3642 (2018).

52. N. G. Bastús, F. Merkoçi, J. Piella, V. Puntes, Synthesis of highly monodisperse citrate-stabilized silver nanoparticles of up to 200 nm: Kinetic control and catalytic properties. *Chem. Mater.* **26**, 2836–2846 (2014).

53. X. Ye, C. Zheng, J. Chen, Y. Gao, C. B. Murray, Using binary surfactant mixtures to simultaneously improve the dimensional tunability and monodispersity in the seeded growth of gold nanorods. *Nano Lett.* **13**, 765–771 (2013).

54. H. Lin, L. Song, Y. Huang, Q. Cheng, Y. Yang, Z. Guo, F. Su, T. Chen, Macroscopic Au@PANI core/shell nanoparticle superlattice monolayer film with dual-responsive plasmonic switches. *ACS Appl. Mater. Interfaces* **12**, 11296–11304 (2020).

55. L. Pan, S. Sun, L. Zhang, K. Jiang, H. Lin, Near-infrared emissive carbon dots for two-photon fluorescence bioimaging. *Nanoscale* **8**, 17350–17356 (2016).

56. T. Zhang, Q. Zhang, J. Ge, J. Goebl, M. Sun, Y. Yan, Y. Liu, C. Chang, J. Guo, Y. Yin, A self-templated route to hollow silica microspheres. *J. Phys. Chem. C* **113**, 3168–3175 (2009).

57. Q. Shi, D. E. Gómez, D. Dong, D. Sikdar, R. Fu, Y. Liu, Y. Zhao, D.-M. Smilgies, W. Cheng, 2D freestanding Janus gold nanocrystal superlattices. *Adv. Mater.* **31**, e1900989 (2019).

58. S. Pekdemir, I. Torun, M. Sakir, M. Ruzi, J. A. Rogers, M. S. Onses, Chemical funneling of colloidal gold nanoparticles on printed arrays of end-grafted polymers for plasmonic applications. *ACS Nano* **14**, 8276–8286 (2020).

59. T. Udayabhaskararao, T. Altantzis, L. Houben, M. Coronado-Puchau, J. Langer, R. Popovitz-Biro, L. M. Liz-Marzán, L. Vuković, P. Král, S. Bals, R. Klajn, Tunable porous nanoallotropes prepared by post-assembly etching of binary nanoparticle superlattices. *Science* **358**, 514–518 (2017).

60. K. Wang, H. Ling, Y. Bao, M. Yang, Y. Yang, M. Hussain, H. Wang, L. Zhang, L. Xie, M. Yi, W. Huang, X. Xie, J. Zhu, A centimeter-scale inorganic nanoparticle superlattice monolayer with non-close-packing and its high performance in memory devices. *Adv. Mater.* **30**, e1800595 (2018).